RESEARCH ARTICLE

# Three-dimensional flow structures and associated turbulence in the tip region of a waterjet pump rotor blade

Huixuan Wu · David Tan · Rinaldo L. Miorini · Joseph Katz

**Abstract** Stereo particle image velocimetry measurements focus on the flow structure and turbulence within the tip leakage vortex (TLV) of an axial waterjet pump rotor. Unobstructed optical access to the sample area is achieved by matching the optical refractive index of the transparent pump with that of the fluid. Data obtained in closely spaced planes enable us to reconstruct the 3D TLV structure, including all components of the mean vorticity and strain-rate tensor along with the Reynolds stresses and associated turbulence production rates. The flow in the tip region is highly three-dimensional, and the characteristics of the TLV and leakage flow vary significantly along the blade tip chordwise direction. The TLV starts to roll up along the suction side tip corner of the blade, and it propagates within the passage toward the pressure side of the neighboring blade. A shear layer with increasing length connects the TLV to the blade tip and initially feeds vorticity into it. During initial rollup, the TLV involves entrainment of a few vortex filaments with predominantly circumferential vorticity from the blade tip. Being shed from the blade, these filaments also have high circumferential velocity and appear as swirling jets. The circumferential velocity in the TLV core is also substantially higher than that in the surrounding passage flow, but the velocity peak does not coincide with the point of maximum vorticity. When entrainment of filaments stops in the aft part of the passage, newly forming filaments wrap around the core in helical trajectories. In ensemble-averaged data, these filaments generate a vortical region that surrounds the TLV with vorticity that is perpendicular to that in the vortex core. Turbulence within the TLV is highly anisotropic and spatially non-uniform. Trends can be traced to high turbulent kinetic energy and turbulent shear stresses, e.g., in the shear layer containing the vortex filaments and the contraction region situated along the line where the leakage backflow meets the throughflow, causing separation of the boundary layer at the pump casing. Upon exposure to adverse pressure gradients in the aft part of the passage, at 0.65–0.7 chord fraction in the present conditions, the TLV bursts into a broad turbulent array of widely distributed vortex filaments.

## List of symbols

| | |
|---|---|
| $c$ | Tip chord |
| $R$ | Casing radius |
| $s$ | Chordwise coordinate |
| $S_{ij}$ | Phase-averaged strain-rate tensor |
| $u_i$ | Instantaneous velocity |
| $U_i$ | Phase-averaged velocity |
| $u_i^{'} = u_i - U_i$ | Velocity fluctuation |
| $k$ | Turbulent kinetic energy |
| $z, r, \theta$ | Axial, radial, circumferential coordinate |
| $\sigma = 2(p_{\text{in.pump}} - p_{\text{vapor}})\rho^{-1}U_{\text{TIP}}^{-2}$ | Cavitation parameter |
| $\omega_i$ | Instantaneous vorticity |
| $\langle\rangle$ | Phase (ensemble) average |

## Subscripts

$z, r, \theta$    Axial, radial, circumf. component

H. Wu · D. Tan · R. L. Miorini · J. Katz (✉)
Department of Mechanical Engineering,
The Johns Hopkins University, Baltimore, MD, USA
e-mail: katz@jhu.edu

H. Wu
e-mail: hwu22@jhu.edu

# 1 Introduction

The adverse effects of tip leakage flows and resulting TLV on the performance and efficiency of turbomachines have been known for quite a while (Cumpsty 1989; Denton 1993; Lakshminarayana 1970, 1996). The TLV effectively blocks part of the blade passage (Khalid et al. 1999), enhances mixing (Li and Cumpsty 1991a, b), and contributes to noise and vibrations (Fukano and Jang 2004; Mailach et al. 2001). The tip leakage and TLV are also believed to be the primary cause of stall onset (Adamczyk et al. 1993; Hathaway 2007; Hoying et al. 1999; Tan et al. 2010; Vo et al. 2008), which is a key phenomenon determining the range of stable operation of compressors. For hydraulic machines, the TLV core is typically the first site for cavitation (Arndt 2002; Farrell and Billet 1994; Laborde et al. 1997). Yet, our understanding of dynamic phenomena occurring in the tip region of axial turbomachines is still quite limited despite numerous observations and numerical simulations, both in linear cascades, e.g., Muthanna and Devenport (2004), Palafox et al. (2008), Wang and Devenport (2004), Wenger et al. (2004), and in rotating turbomachines, e.g., McCarter et al. (2001), Stauter (1993), Xiao et al. (2001). It is known that the tip leakage flow is caused by the pressure difference between the pressure and suction sides of a blade, which forces a backflow through the gap between the blade tip and the casing. Inherently, both the strength and chordwise distribution of this backflow depend on the blade geometry and loading (Lakshminarayana et al. 1982; Miorini et al. 2011; Pouagare et al. 1985). At the point where the backward leakage flow is initiated, the vorticity embedded in the leakage flow rolls up into a TLV (Lakshminarayana 1970), which originates near the suction side (SS) corner of the blade. Its location is greatly affected by the tip gap size (You et al. 2006). Subsequently, the TLV often migrates to the pressure side (PS) the neighboring blade (Furukawa et al. 1999; Gourdain and Leboeuf 2009; Mailach et al. 2001; Miorini et al. 2011; Wilke and Kau 2004). At the exit from the tip gap, the backward leakage flow creates what appears to be a "wall jet", which initially maintains its axial momentum, but then slows down and as is entrained by the developing TLV and encounters the forward passage flow (Miorini et al. 2011; Wu et al. 2011). As long as the TLV is located in the middle of the passage, the wall jet separates from the endwall boundary layer, and it is entrained into the periphery of the TLV. In the aft part of the passage, as the TLV reaches the PS edge of the neighboring blade, the backward flow extends over the entire passage and contributes to the gap flow of the next blade.

Although simplified models have been successful in describing the gross effects of the TLV, such as efficiency losses (Lakshminarayana 1970, 1996), they cannot predict its unsteady features, such as those associated with turbulence production as well as the origin and development of flow instabilities. These instabilities are believed to be primary sources of stall, and sometimes they cause vortex breakdown within the rotor passage (Furukawa et al. 1999; Miorini et al. 2011; Yu and Liu 2007), a phenomenon that totally changes the vortex structure (Hall 1972; Leibovich 1978), as demonstrated in this paper as well. As a general comment, lack of detailed information on the entire flow structure in the passage has been a major obstacle in interpreting limited information obtained experimentally. Consequently, recent efforts to understand the tip leakage and TLV dynamics and their relationships to the onset of stall have shifted to numerical simulations, e.g., Adamczyk et al. (1993), Crook et al. (1993), Gerolymos and Vallet (1999), Vo et al. (2008), You et al. (2006), including studies involving endwall casing treatment to extend the stall margin, e.g., Beheshti et al. (2004), Gourdain and Leboeuf (2009), Guemmer et al. (2008), Hall and Delaney (1994), Hathaway (2007), Schnell et al. (2011), Shabbir and Adamczyk (2005), Wilke and Kau (2004). However, since both RANS and LES involve modeling of all or part of the turbulence, respectively, the reliability of the computational results depends on the validity and applicability of the chosen turbulence closure model along with grid resolution. Consequently, even the most sophisticated computational tools used in turbomachinery require experimental validation. Detailed measurements of the three-dimensional flow structure and turbulence in the tip region are still essential, both as direct evidence of the actual flow phenomena and as benchmark data for validating the computational results.

A few recent studies have attempted to perform experimental validation of numerical results by using particle image velocimetry (PIV) to measure the flow at the tip region of the blade passage, especially with casing treatment installed (Schnell et al. 2011; Voges et al. 2011). Limited optical access to the machine rotor and stator helps to confirm the existence of local flow phenomena, but it does not allow a complete tracking of broad structures and instabilities within the passage. It also cannot pinpoint at causes for quantitative discrepancies between experimental and numerical results, whose origins might be located outside of the field of view. The complexity of the flow in the tip region of turbomachines, e.g., Gbadebo et al. (2005), Gbadebo et al. (2007), Inoue et al. (2001), Mailach et al. (2001), and its inherent unsteadiness require a complete view on the flow structure. Most of the presently available experimental data for turbomachines have been obtained using point sensors (Houghton and Day 2011; Smith and Cumpsty 1984; Stauter 1993; Xiao et al. 2001) but they are difficult to implement within rotating blade

passages and cannot resolve unsteady structures without some conditional averaging. For the first time, the introduction of PIV has provided means to obtain instantaneous snapshots of the flow structure and, indeed, it has already been applied to study the flow and turbulence within the tip region of turbomachine rotors. For example, Liu et al. (2004) use stereo PIV data to examine the evolution of a TLV and the unsteady flow induced by it at near-stall condition. In a later paper, the same team also presents data on TLV breakdown (Yu and Liu 2007). As is evident from these investigations, the primary impediment to the choice of PIV in turbomachinery investigations is optical interference by the blades and casing, which limits the visual access surfaces due to reflections that overwhelm the particle traces. To overcome this limitation, our group has developed an optical index-matched facility, in which both the casing and blades are made of acrylic whose optical refractive index is matched with that of the pumped liquid (Uzol et al. 2002; Uzol et al. 2003). Therefore, the PIV laser sheet can illuminate any desired internal plane within the machine without obstruction or distortion, and the investigated area is optically accessible from multiple points of view. This setup has been used for elucidating a series of flow and turbulence phenomena associated with wake–blade and wake–wake interactions in axial turbomachines, e.g., Chow et al. (2005), Soranna et al. (2006, 2008, 2010), Uzol et al. (2003). In recent years, our facility has been upgraded and used for performing high-magnification planar PIV measurements of the flow in the tip region of a waterjet pump. With an unobstructed view, we have examined the leakage flow within the tip gap and the development of a tip leakage vortex in the blade passage (Miorini et al. 2011; Wu et al. 2011). Results show that the TLV rollup starts right after the appearance of backward leakage flow. After being formed, the TLV detaches from the blade, but continues to be fed for a while by a series of vortex filaments that are shed from the blade tip and embedded in a shear layer connecting the TLV to the SS edge of the blade.

The present paper provides a much more comprehensive view on the development of the TLV, this time by investigating its three-dimensional structure at the pump best efficiency point (BEP). First, we use cavitation as a convenient mean of visualizing the spatial arrangement of the vortex (Arndt 2002). Then, we perform stereo PIV measurements in a series of meridional planes. Data obtained in closely spaced planes enable us to calculate all the ensemble-averaged vorticity and strain-rate tensor components along with Reynolds stresses. These data reveal several new phenomena about the three-dimensional flow in the tip region, e.g., the important role played by vortex filaments in the TLV dynamics and the processes involved with TLV growth and breakup. They also identify several primary contributors to the highly anisotropic and spatially non-uniform turbulence production within and around the TLV.

## 2 Facility and experimental setup

### 2.1 Optical refractive index-matched pump

The axial waterjet pump is installed inside the test loop illustrated in Fig. 1. When the pump itself is not investigated directly, it is used for driving the flow in several test sections that are installed in this facility. The casing and rotor blades of the pump are made of acrylic whose optical refractive index (1.49) is matched with that of the pumped liquid, a concentrated solution of sodium iodide in water (62–64% by weight). Precise matching is achieved by adjusting both the salt concentration and temperature of the solution during experiments. The specific gravity of this liquid is 1.8 and its kinematic viscosity is $1.1 \times 10^{-6}$ $m^2$ $s^{-1}$ i.e., very close to that of water (Uzol et al. 2002). Because of the index matching, the pump inner volume can be observed from any angle and point of view through wide, flat external surfaces located on the top and side of the casing. The pump geometry is illustrated in Fig. 2, and detailed geometrical and performance parameters are listed in Table 1. The pump rotor is connected by a 50.8 mm diameter shaft to a precision-controlled AC motor that has a maximum power of 44 kW, and it is
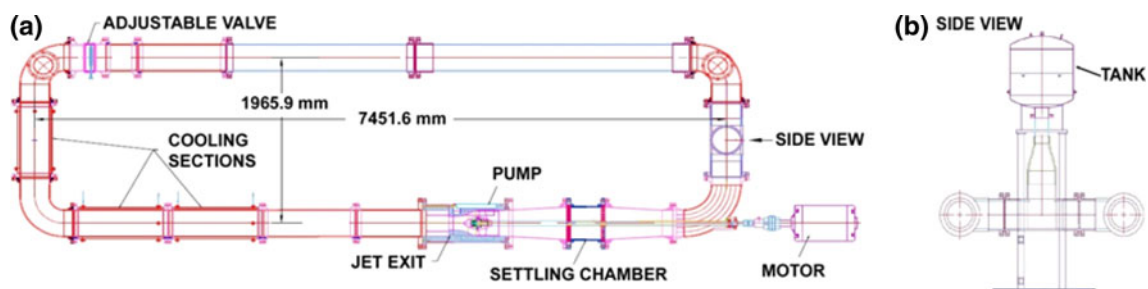


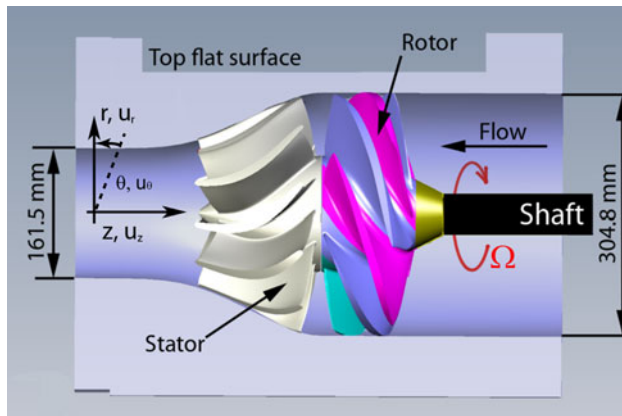**Fig. 1** **a** *Top* and **b** *side* views of the test facility

**Fig. 2** Meridional section of the waterjet pump

**Table 1** Rotor geometry and reference data

| | |
|---|---|
| Number of rotor blades | 7 |
| Number of stator blades | 11 |
| Tip profile chord length $c$ | 267.2 mm |
| Tip profile axial chord length $c_A$ | 74.5 mm |
| Stagger angle $\gamma = \arcsin(c_A/c)$ | 16.2° |
| Rotor diameter $D_R$ | 303.4 mm |
| Casing diameter $D$ | 304.8 mm |
| Span at leading edge | 123.2 mm |
| Span at trailing edge | 79.3 mm |
| Tip clearance (nominal) | 0.7 mm |
| Tip clearance (actual)[a] $h$ | 1.0 mm |
| Clearance to casing diameter ratio $2hD^{-1}$ | $6.6 \times 10^{-3}$ |
| Blade pitch at the tip $\varsigma$ | 136.1 mm |
| Solidity at the tip $c\varsigma^{-1}$ | 1.96 |
| Rotor angular velocity $\Omega$ | 94.2 rads$^{-1}$ (900 rpm) |
| Tip velocity $U_{TIP}$ | 14.36 ms$^{-1}$ |
| Blade chord Reynolds number $Re_c = U_{TIP}\,c\nu^{-1}$ | $3.5 \times 10^6$ |
| Flow rate $Q\{Q\,[0.25\pi(D^2 - d^2_{SHAFT})]^{-1}U_{TIP}^{-1}\}$ | 0.146 m$^3$s$^{-1}$ {0.14} |
| Head rise $H\{gH\,U_{TIP}^{-2}\}$ | 4.2 m {0.20} |
| Flow coefficient $\varphi = Q(\Omega/2\pi)^{-1}D^{-3}$ | 0.34 |
| Head coefficient $\psi = gH(D\Omega/2\pi)^{-2}$ | 1.97 |
| Torque coefficient $k_T = T\rho^{-1}(\Omega/2\pi)^{-2}D^{-5}$ | 0.15 |
| Efficiency $\eta = \rho gHQ(T\Omega)^{-1}$ | 0.74 |
| Inflow Reynolds number $Re_{IN} = QD\,[0.25\pi(D^2 - d^2_{SHAFT})\nu]^{-1}$ | $5.7 \times 10^5$ |

[a] At the measured blade, due to rotor eccentricity

situated outside of the test loop. The shaft penetrates the inlet pipe through a cooled bearing and then passes through a settling chamber containing two honeycombs. Their purpose is to reduce the flow non-uniformities and large-scale turbulence at the pump inflow section.

The rotor has a constant tip diameter, but as the hub diameter increases, the blade span decreases monotonically from 123.2 mm at its leading edge (LE) to 79.3 mm at its trailing edge (TE). Downstream of the rotor, a stator is fitted inside a nozzle whose diameter decreases from 304.8 to 161.5 mm. The nominal width of the tip clearance is 0.7 mm. However, due to a slightly eccentric mounting of the rotor on the shaft, and difference between the designed and manufactured blades, the directly measured tip gap varies between 0.9 and 1.1 mm. We have performed the measurements in an area with a 1.0 mm gap. The clearance to chord ratio is $3.7 \times 10^{-3}$, and the clearance to maximum tip profile thickness is 0.09. The pump can be operated at different working conditions by adjusting the resistance of the loop using a rotating disk valve. This valve consists of an easily replaceable pair of perforated disks; the throughflow blockage is controlled by rotating them relative to each other. The flowrate is measured with an external transit time acoustic flowmeter, and the pressure rise across the pump is measured by connecting taps to a pressure transducer. The measured performance curves of the pump are presented in Fig. 3, which also highlights the flow condition selected for presented Stereo particle image velocimetry (SPIV) measurements. The data have been recorded at the best efficiency point (BEP) flowrate. All the measurements have been performed at 900 rpm, corresponding to a blade tip speed of 14.36 ms$^{-1}$.

### 2.2 PIV setup

Our measurements have been performed in meridional planes, as illustrated in Fig. 4, while the optical setup and orientation of the specific planes interrogated during the
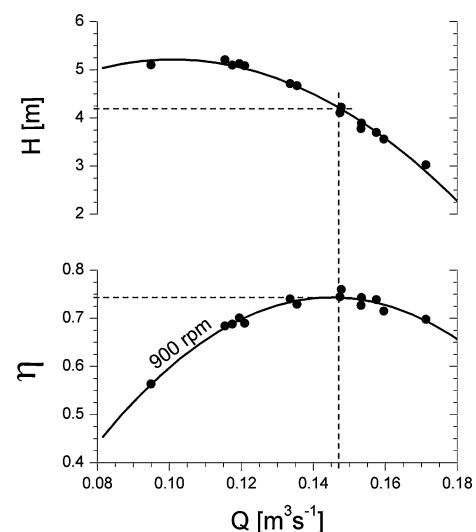


**Fig. 3** Head rise and efficiency curves for the pump. The tested condition is highlighted by a *dashed line*
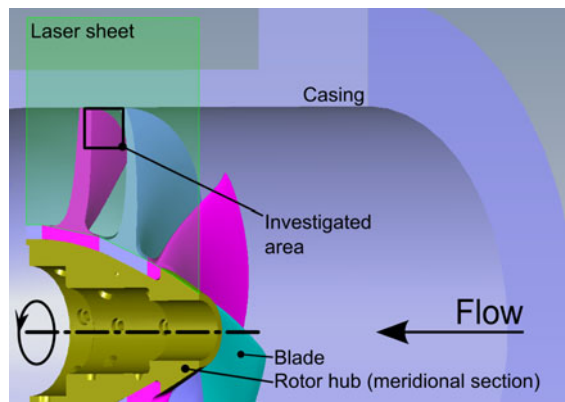
**Fig. 4** Laser sheet configuration and investigated area during SPIV measurements
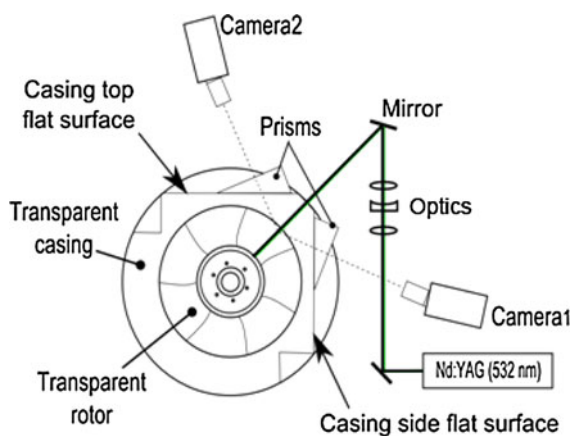


**Fig. 5** Axial section of the pump showing the SPIV optical setup with cameras focusing on the tip region of the rotor blade

present SPIV measurements are presented in Fig. 5. Here, the 1-mm thick Nd:YAG laser sheet (532 nm) illuminates a meridional plane that is oriented at 45° relative to the vertical plane. Two 2,048 × 2,048 pixels CCD cameras are located symmetrically on both sides of the illuminated plane and view the sample area through acrylic prisms whose external surfaces are perpendicular to the optical axes of the camera lenses. Both camera lenses are inclined to the CCD array by the Scheimpflug angle (Prasad 2000). Both cameras focus on the same 30.3 × 32.8 mm sample area, which covers a substantial fraction of the blade passage. As illustrated in Fig. 4, part of two consecutive blade sections is visible in the same image. The cameras, prisms, and laser sheet optics are all mounted on a single rigid structure, which includes a motorized traversing system. It is needed for precisely displacing the entire optical system from the sample area to a calibration chamber (not shown) containing index-matched fluid, which is located above the test section and mimics the sample volume. Calibration of the spatially varying magnification is performed by placing

a custom-made target inside a chamber and following procedures described in Wieneke (2005).

For tracers, we use silver-coated hollow glass spheres that have a mean diameter of 13 μm and a specific gravity of 1.6, i.e., slightly lower but close to that of the fluid. The particle concentration is adjusted to ensure that each 32 × 32 pixel interrogation window contains at least five tracers. Prior to velocity calculation, images are pre-processed by removing non-uniformities in the background light intensity using a median-subtraction filter, followed by the application of a Modified Histogram Equalization (MHE) algorithm, which enhances the contrast (Roth and Katz 2001; Roth et al. 1999), and Gaussian blur filtering. Due to slight mismatch in refractive indices, intersection of the light sheet with blade sections is still visible in the PIV images as faint contour lines. These lines help in measuring the exact blade cross-section but are masked out prior to velocity calculations. Multi-pass cross-correlation of image pairs is performed using an FFT-based software (LaVision© Davis). For the present data, the final interrogation window size is 32 × 32 pixel. Data are obtained with 50% overlap between neighboring windows, providing a vector spacing of 16 pixels, which corresponds to a 0.24-mm in-plane resolution. The typical uncertainty in measurement displacement is about 0.1–0.15 pixels (Roth and Katz 2001; Roth et al. 1999), corresponding to 1.25–2% of the measured value. After ensemble averaging, the mean flow quantities are an order of magnitude more accurate.

In order to phase-lock the timing of measurements with the orientation of the rotor, laser pulses are synchronized with the signal of an encoder mounted on the shaft. The rotor angular position is controlled by varying the time delay between reference signals provided by the encoder and the first laser pulse in a pair. Figure 6 illustrates the rotor tip profile and the method used to indicate the plane where the velocity is measured, i.e., the chord fraction $sc^{-1}$. We use the same axial and radial coordinates for all planes, with $sc^{-1} = 0$ located at the blade LE and $rR^{-1} = 1$ at the casing of the pump. At least 1,000 instantaneous velocity distributions are recorded and then phase-averaged in each sample plane to obtain ensemble-averaged distributions of flow and turbulence quantities, such as velocity, vorticity, strain rate, Reynolds stresses, and turbulent kinetic energy. Successive data acquisitions in the same location are separated by at least four rotor cycles, which is sufficient for obtaining statistically independent data. To obtain data on all six components of the mean velocity gradient in selected areas, we record data in ten closely spaced meridional planes that are separated by a circumferential distance of 0.28 mm at the casing and 0.25 mm at the bottom of the field of view, i.e., by about one quarter of the thickness of the light sheet. This arrangement assures the same spatial resolution in all
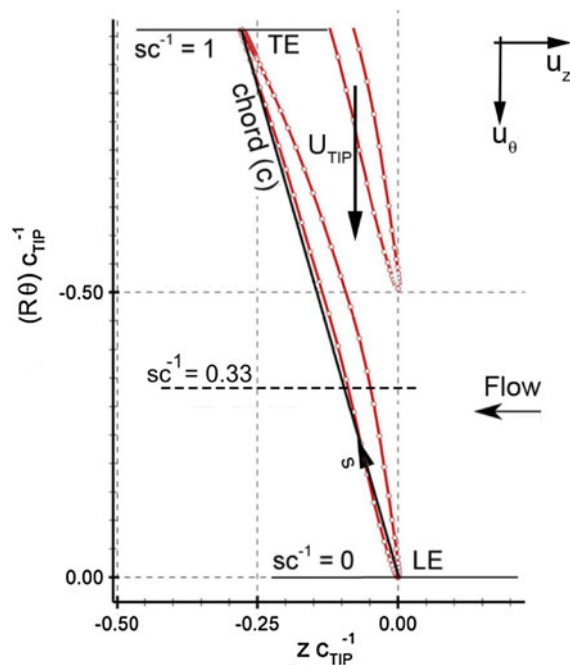
**Fig. 6** Geometry of the tip profile and definition of the chord fraction $sc^{-1}$

directions. As shown in the following sections, these datasets have been instrumental in providing us with a complete view of the 3D flow structure. Divergence of mean velocity field in the three sets of closely spaced meridional planes gives direct estimation of the measurement accuracy. In our data, the root-mean-square of the velocity divergence distribution in the domain is approximately 5% of the maximum normal strain-rate magnitude.

## 3 3D flow structures and associated turbulence

### 3.1 Tip gap flow structures

In recent papers (Miorini et al. 2011; Wu et al. 2011), we have used 2D PIV data sampled in the same pump, but at slightly different operating conditions, to show that the TLV starts developing along the suction side of the blade tip and then migrates across the passage to the pressure side of the neighboring blade. Along its path, the vortex initially grows while entraining vortex filaments that are being shed from the blade tip and form a shear layer that connects the TLV to the suction side corner. In the aft part of the blade passage, vortex busting occurs, which spreads the circulation and turbulence over a broad area. This dataset only includes sparsely spaced planes with distributions of radial and axial velocity components and the circumferential vorticity. Consequently, significant elements of the flow structure are missing there, as the present complete

description of the 3D flow demonstrates. In this paper, we examine three regions, the first one is located at $sc^{-1} = 0.33$, very close to the inception point of the TLV, the second one is located at $sc^{-1} = 0.67$, in a region where, according to our previous results, the TLV has reached its full strength and starts breaking up, and the third is located at $sc^{-1} = 0.89$, well downstream of the vortex breakup region.

The flow in the blade tip region is highly three-dimensional, and characteristics of this flow vary substantially along the chordwise direction. At the BEP flow condition, the backward leakage flow becomes noticeable starting from $sc^{-1} = 0.27$ (not shown). At $sc^{-1} = 0.33$, there is already a clearly defined TLV near the SS corner. Figure 7a shows all three components of the mean velocity of this newly forming vortex with the in-plane velocity components, i.e., axial and radial, indicated by arrows. The circumferential component is displayed as a color contour. The corresponding circumferential vorticity is presented in Fig. 7b, and sample instantaneous velocity and vorticity distributions of the flow are presented in Fig. 7c, and d, respectively. In this plane, the phase-averaged circumferential (out-of-plane) velocity, $U_\theta$, peaks near the SS edge of the blade, reaching 31% of the tip speed (Fig. 7a, point A), in the region where the boundary layer develops along the blade tip within the tip gap and detaches from the blade. When the leakage flow emerges from the tip gap, it forms an angle with respect to the meridional plane that varies from 30° close to the endwall to 55° near the SS corner, where the axial backflow velocity, not shown, is about 27% of the tip speed. The circumferential velocity decreases to about 23% of the tip speed at the center of the TLV (point B), where the point of maximum $\langle \omega_\theta \rangle = \partial_z U_r - \partial_r U_z$ (mean circumferential vorticity) is marked by a circle. As is evident from Fig. 7a and b, the local vorticity peak does not coincide with a local maximum in circumferential velocity. Still, relative to the surrounding flow, during rollup, in the stator frame of reference, the phase-averaged TLV appears like an out-of-plane swirling jet. The fact that tip vortices are inherently three-dimensional and involve out-of-plane motion relative to the surrounding flow has already been established also based on theoretical arguments (Batchelor 1967; Saffman 1992). In the instantaneous sample, the TLV core is composed of two or three co-rotating swirling jet-like vortex filaments, and another one is being shed from the blade tip. These vortices never fully merge within the blade passage, and, as shown below, complex interactions among filaments that are being continuously shed from the blade tip play key roles in the TLV flow dynamics. Such interactions have been observed also in external flows involving co- and counter-rotating vortices, e.g., Batchelor (1967) and Ortega et al. (2003). At $sc^{-1} = 0.33$, the mean tip leakage backflow penetrates into
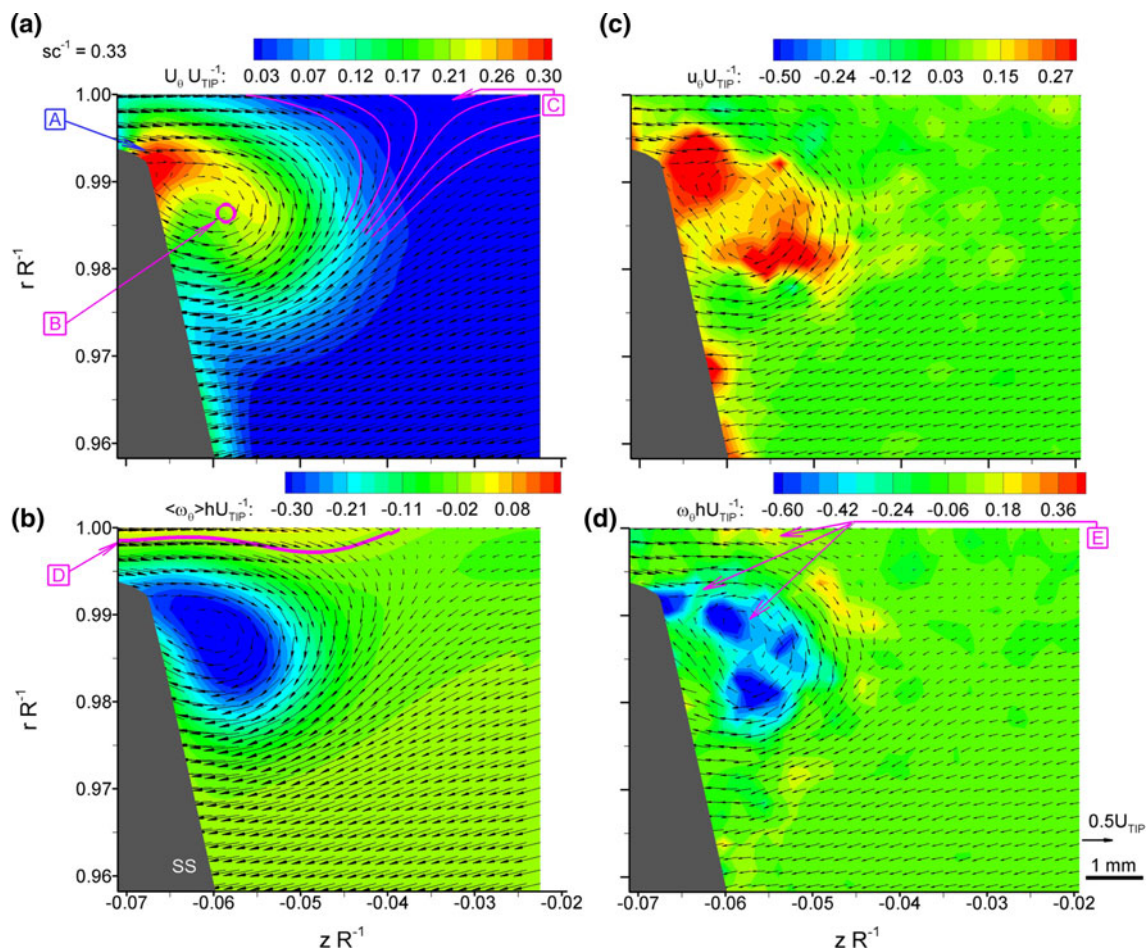
**Fig. 7** Plane view of instantaneous and phase-averaged circumferential velocity and vorticity distributions on the meridional plane at $sc^{-1} = 0.33$. **a** Phase-averaged velocity field with vectors showing axial and radial components, contour showing circumferential component, **b** phase-averaged circumferential vorticity, **c** a sample instantaneous velocity map, and **d** associated circumferential vorticity. *A* peak of circumferential velocity, *B* mean TLV center, *C* separation point highlighted by streamlines, *D* line of zero circumferential vorticity, and *E* counter-rotating vortex filaments

the blade passage up to point C (Fig. 7a), where it meets the main passage flow, and the boundary layer developing on the pump casing separates from the endwall.

At $sc^{-1} = 0.67$, the TLV is fully developed and has migrated to the center of the blade passage as illustrated by the distribution of mean velocity components (Fig. 8a, b) together with instantaneous snapshot of velocity (Fig. 8c) and circumferential vorticity (Fig. 8d). A sketch of the mean vorticity orientation in the TLV (Fig. 8e) is generated after a careful analysis of the averaged three-dimensional vorticity distribution, whose components are shown in Fig. 8f, g, h. Here, the region of high mean circumferential velocity extends from the blade SS tip and wraps around the now developed TLV core, whose circumferential vorticity center is again marked with a circle. A perspective view of the velocity distribution (Fig. 8a) is presented to emphasize the spatial non-uniformity of the circumferential velocity component. Here, the velocity contours are drawn over a surface that protrudes out of the

meridional plane proportionally to the local magnitude of $U_\theta$. This plot highlights that the shear layer extending from the SS corner and feeding vorticity into the TLV core actually jets out from the tip gap with a high circumferential velocity and is characterized by high radial gradients of both the axial and circumferential velocity components. Above the TLV center, the circumferential velocity decreases, but then it increases again to form a broad region with high $U_\theta$ to the right of and below the TLV center. Thus, the high $U_\theta$ below the TLV center is not only a result of entraining fluid with high circumferential momentum from the tip gap, as confirmed also by the instantaneous sample in Fig. 8c. The reasons for this phenomenon are described in the following.

The three mean vorticity components (Fig. 8f, g, h) reveal a complex 3D structure. The circumferential vorticity distribution shows regions with high negative $\langle \omega_\theta \rangle$ in the vortex core and in the shear layer feeding it. In addition to those, a region with circumferential vorticity of opposite
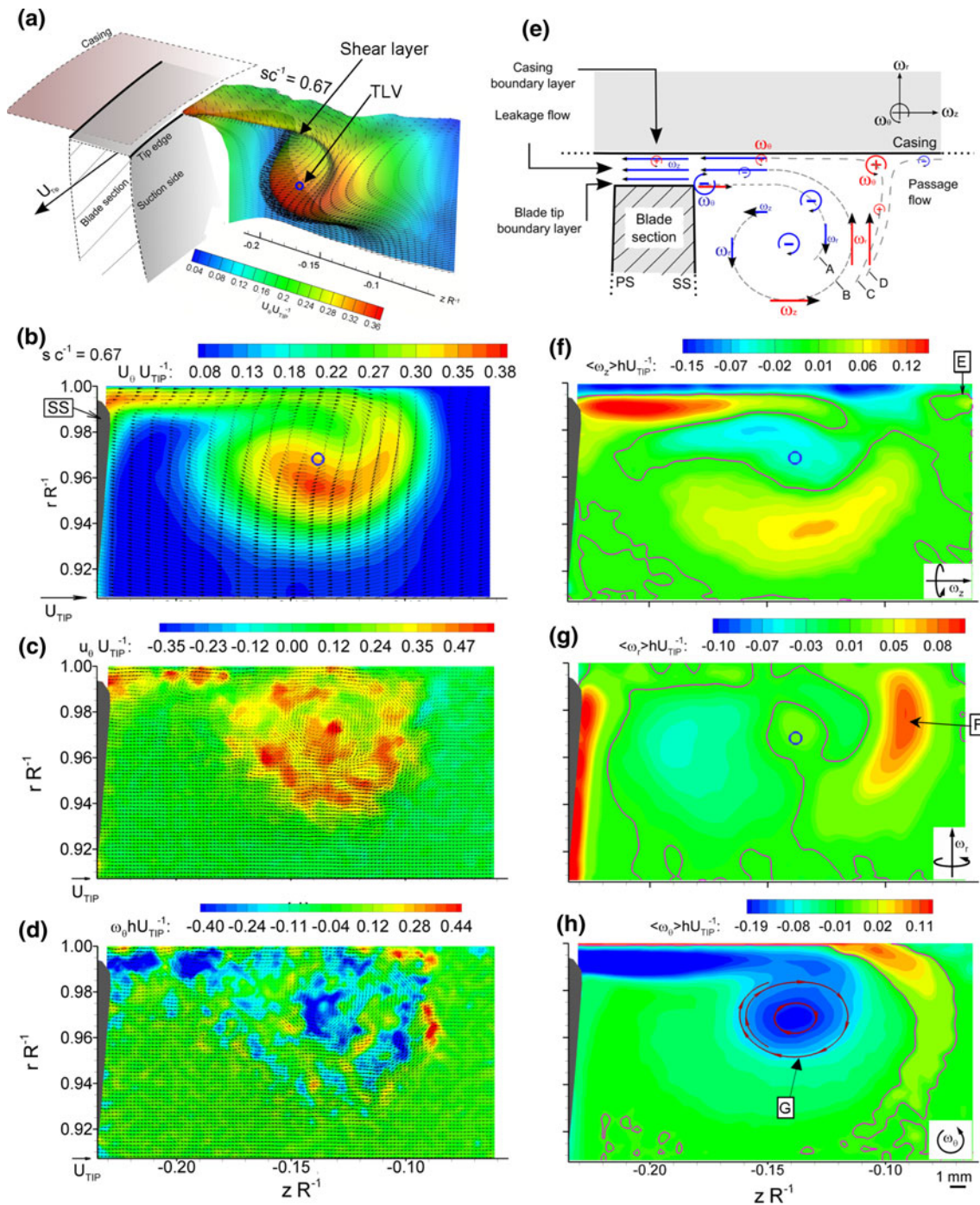
**Fig. 8** Velocity and vorticity distributions in the meridional plane at $sc^{-1} = 0.67$. **a** Perspective view of circumferential velocity distribution with three-dimensional velocity vectors, **b** phase-averaged velocity with vectors showing axial and radial components, contour showing circumferential component, **c** instantaneous velocity snapshot, **d** instantaneous circumferential vorticity **e** sketch of vorticity distribution surrounding the TLV, and **f** axial, **g** radial and **h** circumferential mean vorticity components. *E* line of zero vorticity component. *F* radial vorticity peak. *G* streamlines near the TLV center. Vectors in (**b**) are diluted horizontally 1:5 horizontally for clarity, vectors in (**c**) and (**d**) are not diluted

sign originates from the point of endwall boundary layer separation, where the backward leakage flow meets the main passage flow. This counter-rotating vorticity layer is pulled away from the wall by the TLV and then surrounds

the core, but it is not entrained into it. The instantaneous sample (Fig. 8d) shows again that the flow structure consists of mostly negative, but also a few positive, vortex filaments, many of which are actually swirling jets with

high circumferential velocity (Fig. 8c). Even in this developed state, the TLV clearly does not have a distinct core, but a series of interlacing vortices.

Most striking and puzzling, however, is the picture introduced by the distributions of axial and radial vorticity components in the tip region. Both $\langle\omega_z\rangle = \partial_r U_\theta - r^{-1}(\partial_\theta U_r - U_\theta)$ and $\langle\omega_r\rangle = r^{-1}\partial_\theta U_z - \partial_z U_\theta$ vary substantially and change signs several times. The sketch in Fig. 8e is an attempt to elucidate the origin and evolution of this flow structure. Here, axial and radial vorticity components are indicated by arrows pointing in the direction of the vorticity, while circular arrows rotating appropriately indicate the circumferential vorticity. Red and blue lines indicate positive and negative values, respectively. Within the tip gap, the combination of rotor blade out-of-plane motion and stationary casing fills the entire gap with negative $\langle\omega_z\rangle$. Conversely, $\langle\omega_\theta\rangle$ is positive in the casing boundary layer and negative near the blade tip, and for most of the tip gap. As the tip clearance backflow penetrates the passage, these layers of vorticity follow different paths. Layer C, shown in Fig. 8e, namely, the casing boundary layer, detaches from the casing wall at the point of flow separation and wraps around the outer perimeter of the TLV. As it circumvents the vortex, its $\langle\omega_z\rangle < 0$ becomes $\langle\omega_r\rangle > 0$, while $\langle\omega_\theta\rangle$ maintains the same positive sign. Layer B includes the bulk of the tip gap flow and spirals around the TLV core making more than a complete circle before being entrained into the vortex. It starts with $\langle\omega_z\rangle < 0$ and $\langle\omega_\theta\rangle < 0$ as it leaves the gap. During entrainment, the circumferential vorticity maintains the same sign, but the other two components alternate, changing from $\langle\omega_z\rangle < 0$ above the TLV, to $\langle\omega_r\rangle > 0$ to the right (upstream) of the TLV, to $\langle\omega_z\rangle > 0$ below the vortex, to $\langle\omega_r\rangle < 0$ to the left of it, and finally back to $\langle\omega_z\rangle < 0$ just before being entrained into the vortex center from above. Layer A extends from the tip SS corner and contains fluid entrained from the passage into the lower part of the shear layer. It also has $\langle\omega_\theta\rangle < 0$, but its $\langle\omega_z\rangle$ is positive, mostly due to the positive $\partial U_\theta/\partial r$ in the lower part of the jetting shear layer. This layer is entrained directly into the TLV from its upper side, i.e., it does not spiral. As this layer turns into the TLV, its $\langle\omega_z\rangle > 0$ changes to negative $\langle\omega_r\rangle$, but its circumferential vorticity maintains the same sign. Figure 8e contains also another layer, designated as D, which starts with the endwall boundary layer generated by the passage flow upstream of the separation point. Its negative circumferential vorticity also detaches from the endwall when the boundary layer separates; this vorticity is weak and difficult to detect in the mean flow distribution shortly after separation. The signatures of these changes in orientation are evident in the data presented in Fig. 8f and g, which, if combined, create a continuous entrainment path of layer B. It ought to be emphasized here that the spiraling process around the TLV core is three-dimensional with an out-of-plane (circumferential) velocity that is comparable to the in-plane components (Fig. 8b). Consequently, in a certain meridional plane, for instance, layer C contains fluid that has leaked from the tip gap over a range of lower chord fractions. Fluid passing through the tip gap at lower $sc^{-1}$ appears farther from the SS corner.

The overall impact of layer B is to surround the TLV with vorticity that is perpendicular to the orientation of the TLV centerline. To help in identifying the origin of this vorticity conclusively and confirming the paths illustrated in Fig. 8e, we have visualized the vortices in the tip region by operating the pump at low pressure and observing the physical appearance of cavitation. Several sample snapshots of a high-speed movie are presented in Fig. 9. Figure 9a and b shows the same image of a TLV rolling up and starting to migrate away from the blade SS corner, but in the latter, the TLV is painted blue. The TLV has multiple and visible "kinks" (Fig. 9b, c), which seem to coincide with the places containing helical vortex filaments, highlighted in red in Fig. 9b, to the right of the TLV center. The high-speed movies clearly show that these vortices are filled with vapor and swirl in direction indicated for layer B, i.e., with $\langle\omega_\theta\rangle < 0$, as well as with $\langle\omega_r\rangle > 0$ to the right of the TLV and $\langle\omega_z\rangle > 0$ below it. The locations of these regularly occurring filaments match those of the $\langle\omega_z\rangle$ and $\langle\omega_r\rangle$ peaks in Fig. 8f and g, respectively, and in agreement with their orientation, a fraction of the vorticity within them is aligned in radial and axial directions. The kinks in the main TLV structure develop at the point where these filaments are entrained into the core area, consistent with the sketch drawn in Fig. 8e. Thus, in summary, in the process of entraining the vorticity from the blade tip, a significant fraction of the vortex filaments spiral around the TLV before being entrained into it. Their imprint on the mean vorticity distribution is a vortical coil that surrounds the TLV center, with a substantial fraction of the vorticity perpendicular to its axis. The significance of this phenomenon can be demonstrated by a comparison between Fig. 8f–h. The region with high circumferential velocity just below the TLV center is situated exactly between the positive and negative $\langle\omega_z\rangle$ peaks, as well as between the positive and negative $\langle\omega_r\rangle$ peaks. Thus, the previously mentioned increase in circumferential velocity to the right and below the TLV center is at least in part a result of out-of-plane motion induced by the combined effect of coiling vortex filaments.

In view of the demonstrated flow structure, one might ask why the cavitation appears to the right and below the TLV, but not above it. The answer to this question can be obtained by examining the spatial distribution of normal
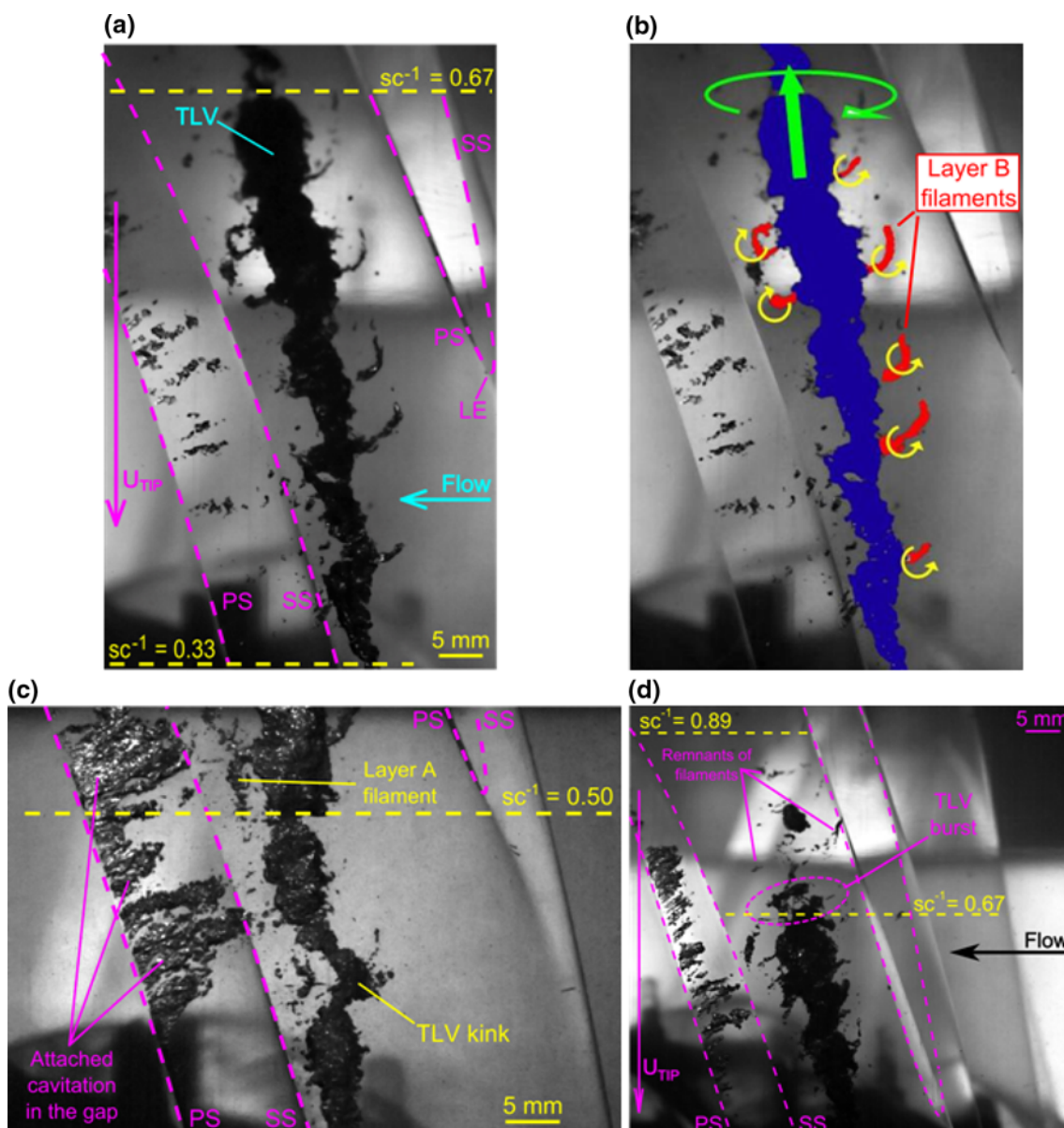
**Fig. 9** Pictures of cavitation associated with the *tip* flow and vortex ($\sigma = 0.21$). The passage flow is to the *left*, and the blade moves down. **a**, **b** Secondary vortex filaments coiling around the TLV, **b** is the same image as (**a**) with the TLV cavitating core colored in *blue* and outer filaments in *red*. *Arrows* on the vortex *center line* indicate the spinning directions. **c** Kinks in the TLV core and the entrained "layer A" filaments. **d** Cavitation image in the aft part of a blade. Remnant filaments reach the PS of following blade after TLV burst

mean strain components, in particular $S_{zz} = \partial_z U_z$ and $S_{\theta\theta} = r^{-1}(U_r + \partial_\theta U_\theta)$, which are presented in Fig. 10. As is evident, along the trajectory of layer B, both $S_{zz}$, and $S_{\theta\theta}$ are positive on the right bottom side of the TLV center, indicating that the vortex filaments are stretched in the region where the cavitating becomes visible. Conversely, $S_{zz}$ is negative, i.e., the flow undergoes contraction, and $S_{\theta\theta}$ is negligible above the TLV. Since stretching of a vortex increases its vorticity and reduces its core pressure, one should expect that cavitation is more likely to occur in a region of vortex stretching, consistent with the present observations. The values of $S_{zz}$ are also positive and

particularly high on the top left corner of the TLV, in the region occupied in part by the layer A filaments. Indeed, intermittent cavitating filaments also appear in this region, as demonstrated in Fig. 9c. These structures are short lived and do not coil around the core, also consistent with their belonging to layer A. Note that the velocity induced by these rings is consistent with the elevated circumferential velocity below the TLV center, i.e., they contribute to the out-of-plane circumferential velocity gradients. Before proceeding, one should also note that all of the images in Fig. 9 show that attached cavitation develops in the tip gap, creating bubbly tracks that move with the blades.
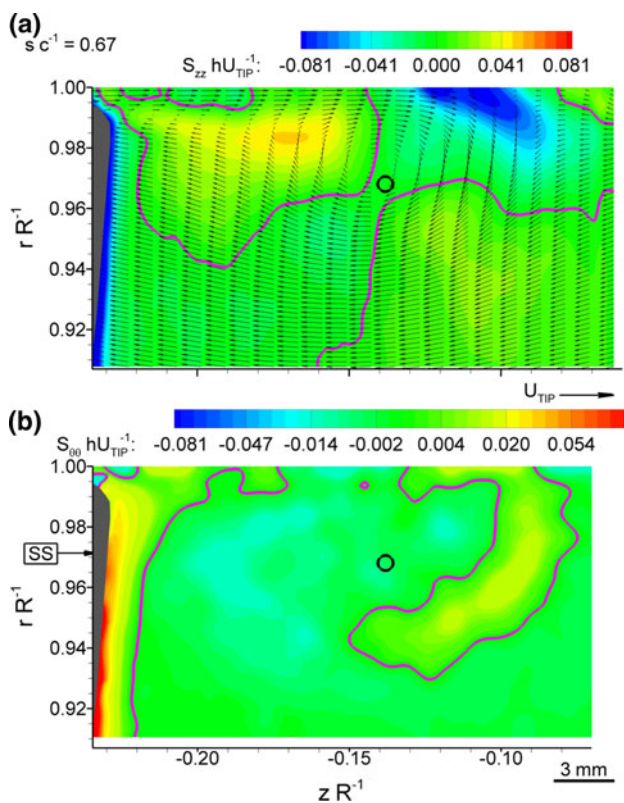
**Fig. 10** Selected normal strain-rate components **a** $S_{zz}$, **b** $S_{\theta\theta}$ at $sc^{-1} = 0.67$. *Black circles* mark the TLV center. Velocity vectors are diluted 1:5 *horizontally* for clarity. Contour lines indicate zero strain-rate component

Around $sc^{-1} = 0.7$, the cavitation within the central part of the TLV stops abruptly, as Fig. 9d demonstrates, leaving only a few remnants of the spiraling filaments that no longer have a helicoidal trajectory. Some of these filaments migrate to the PS of the neighboring blade and are typically aligned in the axial direction. The disappearance of cavitation in the main TLV core can only occur as a result of rapid increase in pressure within vortices that are located in the vicinity of the TLV core. Vortex bursting, as reported also for other turbomachines (Kosyna et al. 2005; Schrapp et al. 2004; Yu and Liu 2007), is the most likely phenomenon that could cause an abrupt increase in vortex core size and corresponding localized increase in pressure.

The impact of this breakup on the tip region flow structure at $sc^{-1} = 0.89$ is demonstrated in Fig. 11. In this plane, the TLV has already migrated to the pressure side of the neighboring blade. The jetting shear layer emerging from the tip gap is still evident in Fig. 11a, but the backward wall jet extends over the entire passage, and merges with the leakage flow of the next blade (Fig. 11b). Since there is no endwall casing boundary layer separation, the negative $\langle\omega_z\rangle$ layer generated in the tip gap remains close to the casing across the entire passage. Associated layers with elevated $\langle\omega_z\rangle$ of opposite signs, as discussed before,

can be seen in Fig. 11e. Based on the distribution of mean circumferential vorticity (Fig. 11g), as a result of bursting, the mean TLV core area quadruples, and the peak vorticity magnitude near the TLV center decreases to $\sim 50\%$ of its pre-breakup level. Nonetheless, the overall circulation of the TLV mildly remains the same from $sc^{-1} = 0.67$ to $sc^{-1} = 0.89$. The circulation is calculated by integrating the circumferential vorticity $\langle\omega_\theta\rangle$ over the area where it exceeds $e^{-1}$ time the TLV peak $\langle\omega_\theta\rangle$ value. Therefore, the TLV does not entrain additional vorticity after $sc^{-1} = 0.67$ and is consistent with our previous findings (Miorini et al. 2011). Additional vortex filaments that are shed from the blade remain within the shear layer. Examination of streamlines in the meridional plane around the TLV core reveals that during the initial rollup, they converge spirally inward (not shown), indicating vorticity entrainment and increased spin of the core. For the present BEP condition, at $sc^{-1} = 0.67$, the streamlines surrounding the core are already closed, i.e., mean entrainment has already ceased, while streamlines far away from the TLV center start to gradually unwind (Fig. 8h). At $sc^{-1} = 0.89$, as demonstrated in Fig. 11g, the mean streamlines spiral outward, i.e., the mean TLV core is expanding, and is not entraining additional structures. Being located in the aft part of the rotor passage, the circumferential velocity increases in a stationary frame, i.e., decreases relative to the blade, over the entire blade passage. Figure 11b indeed confirms this trend, but also shows that in the vicinity of the TLV core, the increase in $U_\theta$ is significantly higher than that in the surrounding passage. This trend is also consistent with the growth in vortex core size and the increase in pressure, as demonstrated by the termination of cavitation, all presumably due to the vortex breakup. The instantaneous samples (Fig. 11c and d) confirm that the vicinity of the TLV contains multiple, widely distributed vortex structures but, unlike the flow prior to breakup, the vicinity of the TLV core, i.e., the point where $\langle\omega_\theta\rangle$ peaks, already shows a compact region with elevated circumferential vorticity and high circumferential velocity. Around it, there are several "satellites," each consisting of multiple structures, and each having high circumferential velocity, e.g., the one situated around $zR^{-1} = -0.19$, $rR^{-1} = 0.93$. These "satellites" are groups of vortices that can no longer be entrained into the core. Therefore, they swirl around a common center, filling in the passage and even reaching the nearby blade. In the corresponding mean distributions, the center of the broad peak in $U_\theta$ (Fig. 11a and b), which is now situated only slightly below the TLV center, covers the space occupied by the central vortex along with the satellite structures.

Distributions of in-plane vorticity components are shown in Fig. 11e, f, g; they display signs of the previously discussed vortex ring that surrounds the TLV core. In this
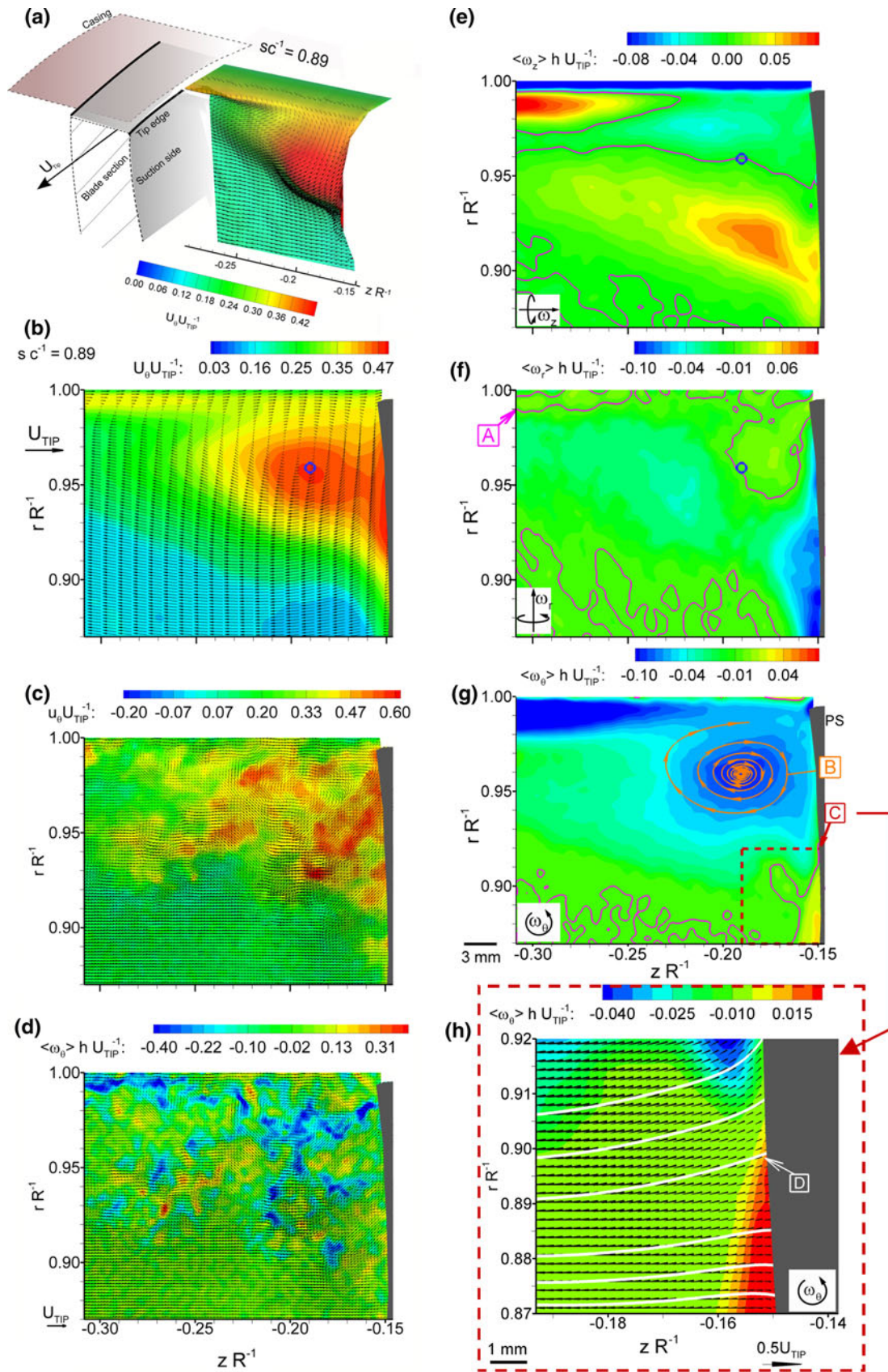
plane that region is associated with the spiraling satellites. In addition, interactions of the TLV with the boundary layer on the pressure side of the neighboring blade introduce new phenomena shown in Fig. 11h. First, a vortex-induced negative radial velocity develops along the blade to the right of the vortex center, causing generation of positive circumferential vorticity on the surface of the blade. Second, the vortex-induced flow causes boundary layer separation on the PS of blade slightly below the TLV, at $rR^{-1} = 0.89$. The separated flow carries with it both the above-mentioned positive $\langle \omega_\theta \rangle$ as well as negative radial vorticity that is inherently generated in the boundary layer at the PS of the blade. Third, wall-induced blockage constrains the path of the satellite structures between the TLV center and the blade, increasing the mean circumferential vorticity outside of the blade boundary layer. Furthermore, the entire space between the TLV and the blade has high $U_\theta$, due in part to the blade boundary layer and in part to the high circumferential velocity within the satellites. Finally, the positive axial vorticity below the TLV, which is associated with the spiraling structures, is exposed to a particularly high positive streamwise normal strain rate (not shown) in the region of flow separation. This axial vortex stretching increases the streamwise vorticity under the TLV.

## 3.2 Turbulence associated with the TLV

A spatially non-uniform and anisotropic turbulence field develops as a result of the complex and interacting flow structures involved with TLV rollup, migration, and breakdown. Although detailed characterization of turbulence is beyond the scope of the present paper, Fig. 12 provides distributions of the turbulent kinetic energy (TKE), $k = 0.5 \left\langle u_z'^2 + u_r'^2 + u_\theta'^2 \right\rangle$, and Fig. 13 shows the very different normal Reynolds stress patterns at $sc^{-1} = 0.67$ only, in order to demonstrate the impact of previously discussed flow features on the turbulence. At $sc^{-1} = 0.33$, the leakage flow feeds elevated turbulence into the blade passage, and new TKE is generated mostly due to shear production as the jetting shear layer starts to develop, as shown in Fig. 12a. The layer with elevated TKE
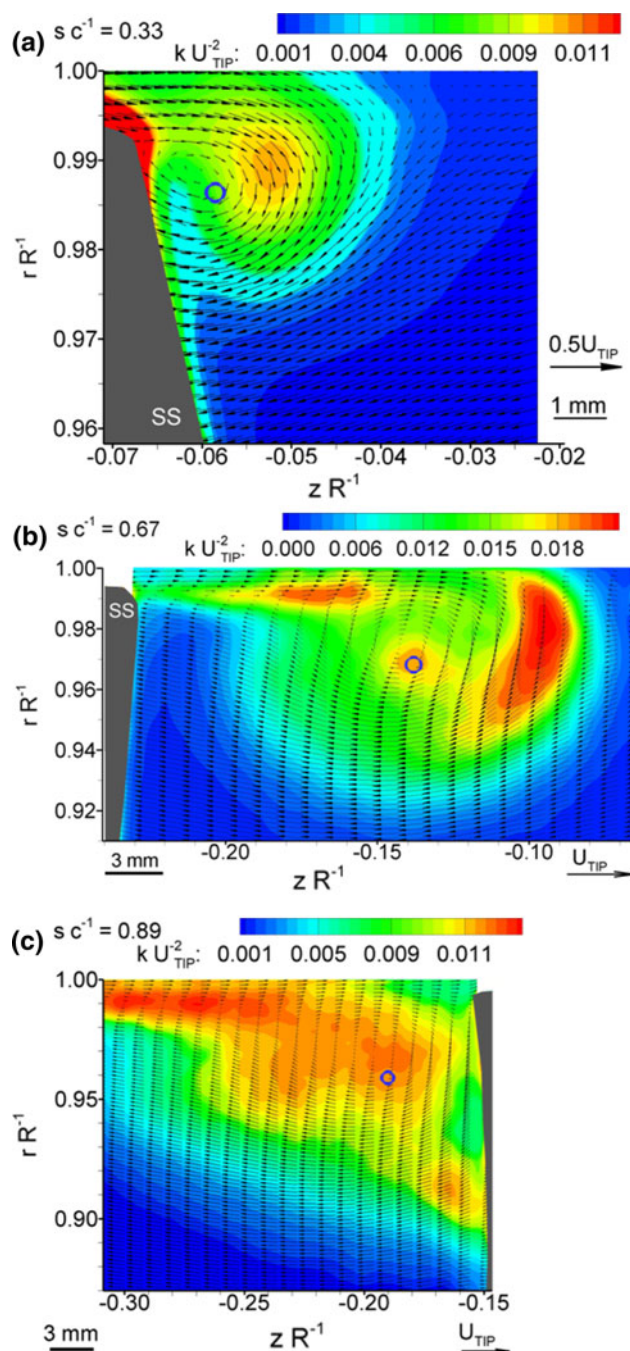


**Fig. 12** Turbulence kinetic energy at $sc^{-1} =$ **a** 0.33, **b** 0.67, and **c** 0.89. *Circles* mark the point of maximum circumferential vorticity within the TLV core. Vectors in (**b**) and (**c**) are diluted 1:5 *horizontally* for clarity, vectors in (**a**) are not diluted

surrounding the TLV center coincides with the high $U_\theta$ layer shown in Fig. 7a.

In the jetting shear layer, $\left\langle u_\theta'^2 \right\rangle$ is by far the largest contributor to the TKE, followed by $\left\langle u_z'^2 \right\rangle$. To identify the flow mechanisms affecting each component, we have examined all the terms in the corresponding Reynolds stress production rates, but opt to defer the plots to future
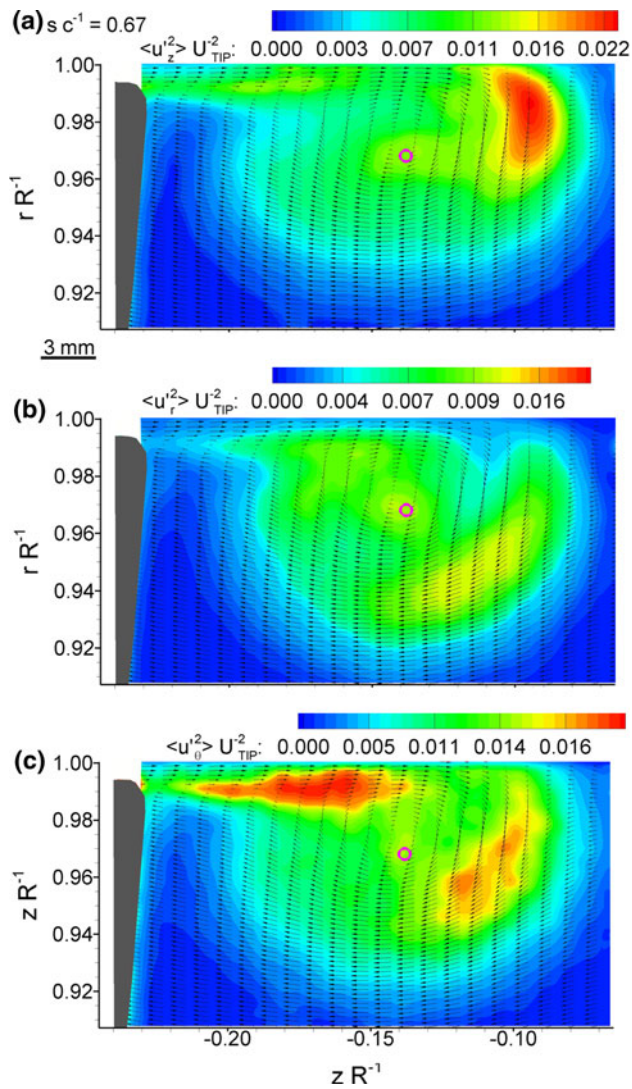
**Fig. 13** Plane view of the Reynolds stresses **a** $\langle u_z'^2 \rangle$, **b** $\langle u_r'^2 \rangle$, **c** $\langle u_\theta'^2 \rangle$ at $sc^{-1} = 0.67$. In-plane velocity vectors are diluted 1:5 *horizontally* for clarity. The *circles* indicate the maximum circumferential vorticity within the TLV core

papers. Within the shear layer, the so-called shear production terms are the main contributors, i.e., $\langle u_z' u_r' \rangle \partial U_z / \partial r$ for the axial stress, and $\langle u_\theta' u_r' \rangle \partial U_\theta / \partial r$ for the circumferential stress, both of which resulting from high radial gradients in the corresponding velocity components. In the region of endwall boundary layer separation, $\langle u_z'^2 \rangle$ is the largest term, mostly due to high flow contraction, i.e., $\partial U_z / \partial z$, in the region where the leakage backflow meets the mean throughflow. As the flow separates, and within layers B and C (Fig. 8e), shear production takes over. Beneath the TLV, in the region containing the cavitating swirling vortex filaments, $\langle u_\theta'^2 \rangle$ is the largest term, but the other components also contribute substantially, all due to in- and out-of-plane shear production. The TKE is also high near the vortex center as a combined effect of all the three

components, while the production rate there is quite low. In Miorini et al. (2011), we use 2D data to show that turbulence is advected into the TLV center as part of the entrainment process of vortex filaments. We also show that ~40% of the TKE is associated directly with meandering vortex filaments.

At $sc^{-1} = 0.89$, the TKE is elevated over a broad area that coincides with the region of high circumferential velocity. The peak values are lower than those measured prior to vortex bursting, and they cover a much larger area. Within this domain, the highest turbulence level still is located within the shear layer, but unsteadiness is also strong in the area located above the TLV core, and in the region of flow separation under the TLV. In general, $\langle u_\theta'^2 \rangle$ is the largest contributor to the TKE, especially in the jetting shear layer, along with $\langle u_z'^2 \rangle$, near the location of flow separation from the blade, and in the region of elevated radial gradients of $U_\theta$, under the high velocity peak. Above the TLV center, both $\langle u_z'^2 \rangle$ and $\langle u_r'^2 \rangle$ are also significant contributors, but at different locations. Each component peaks at distinct areas within the flow contraction region, and the TKE is a combination of both.

## 4 Summary and conclusions

We use stereo PIV data along with observations of the structure of cavitation to follow the development of a tip leakage vortex in an axial waterjet pump rotor, from its initial rollup to breakdown. Inherently, three-dimensional flow structures within and around the TLV vary substantially during the process of vortex development inside the blade passage. The TLV starts to form near the SS edge of a blade tip by entraining vortex filaments shed from the blade tip, and due to the high circumferential velocity in its core, it appears like a swirling jet in a stationary reference frame.

As it grows, the TLV migrates to the middle of the blade passage, while continuing to entrain vortex filaments that are shed from the blade tip. Within the TLV core, the vortex filaments never merge into a single structure, and instantaneous realizations show a series of interlacing filaments wrapped around each other. The backward leakage flow also penetrates deeper into the passage, and its interface with the main forward flow creates a shear layer containing a series of vortex filaments that connect the SS edge of the blade tip with the TLV and feeds it with vorticity. The circumferential velocity in this shear layer is substantially higher than that in the surrounding passage flow, and as a result, it actually appears as a jetting fluid in mean flow profiles and a series of swirling jets in instantaneous realizations. The entrainment process involves

several layers with different orientation of vorticity and different paths, depending on their origin. One of these layers is entrained directly into the TLV, while the other, which is originated from the tip gap, circumvents the TLV and forms a series of helical swirling vortices that surround the core. Stretching of these helical structures makes them prone to cavitation, and their entrainment generates kinks in the TLV core. The signature of these helical structures in mean vorticity distributions appears as a ring that surrounds the core and then merges into it, with vorticity aligned perpendicularly to the TLV axis. The magnitude of this vorticity is in the order of 50% of the circumferential vorticity in the vortex core, i.e., it is not negligible. The flow induced by this ring increases the circumferential velocity significantly in a region located slightly below the TLV center. Another layer forms when the backward leakage flow meets the forward main passage flow and subsequently the endwall boundary layer separates, feeding opposite sign circumferential vorticity that also wraps around the TLV. At this chord fraction, the turbulence level is high in the jetting shear layer, in the separating endwall boundary layer, within the region surrounding the TLV center, and in the vortex core. Several processes are involved with turbulence production (not shown), including shear production both in-plane and out-of-plane, along with contraction of the flow in certain domains.

As the TLV migrates to the pressure side of the neighboring blade, it stops entraining vorticity and starts to unwind, i.e., the core flow spirals outward, initially slowly, but then rapidly. Cavitation in the TLV center disappears abruptly, indicating an increase in TLV core pressure, and the velocity distribution displays a rapid increase in TLV core size, a decrease in circumferential vorticity, and an increase in circumferential velocity. These rapid changes likely imply that vortex breakup/bursting occurs within the blade passage. Once bursting occurs, the broad TLV center is still surrounded by satellite groups of spiraling vortex filaments with high circumferential velocity, which maintain the vortical ring around the vortex center. In this region, the backward leakage flow covers the entire blade-to-blade gap and merges with the leakage flow of the neighboring blade. Interaction of the TLV with this blade also generates inward radial flow and boundary layer separation at the PS surface. In this region, the turbulence level is high over a wide area that covers the still present jetting shear layer, the TLV center, the area covered by the satellite vortices, and in the region of blade boundary layer separation. In the present results, the TLV core mean radius, calculated from the area where the circumferential vorticity exceeds $e^{-1}$ times the peak value, varies from about two to six times the gap size, increasing with chordwise location. Empirical relations developed by Shuba (1983) and adopted by Farrell and Billet (1994),

based on measurements performed downstream of a rotor, predict a TLV radius of $\sim 5\ h$, for the present chord-based Reynolds number, tip gap to blade maximum thickness ratio, and chordlength. Oweis and Ceccio (2005) show a core size of $\sim h$, close to the trailing edge of a propeller with a large $hc^{-1}$ of 1.8%. Thus, all the results fall within the same order of magnitude.

Before concluding, we should note that operating this pump below design conditions shifts the entire process, including rollup, migration, and bursting to a lower chord fraction. Eventually, the entire process occurs before the next blade arrives, and the much more tangential, broken up TLV extends in part to an area located upstream of the rotor blade. Consequently, when the next blade leading edge arrives, it dissects the TLV and immediately feeds spiraling vortex filaments into it near its leading edge. Formation of such spiraling vortex filaments at the leading edge below design conditions has already been observed, e.g., by Kosyna et al. (2005) and Schrapp et al. (2004), i.e., it is not unique to our facility.

# References

Adamczyk JJ, Celestina ML, Greitzer EM (1993) The role of tip clearance in high-speed fan stall. J Turbomach 115:28–39

Arndt REA (2002) Cavitation in vortical flows. Annu Rev Fluid Mech 34:143–175

Batchelor GK (1967) An introduction to fluid dynamics. Cambridge University Press, Cambridge

Beheshti BH, Teixeira JA, Ivey PC, Ghorbanian K, Farhanieh B (2004) Parametric study of tip clearance—casing treatment on performance and stability of a transonic axial compressor. J Turbomach 126:527–535

Chow YC, Uzol O, Katz J, Meneveau C (2005) Decomposition of the spatially filtered and ensemble averaged kinetic energy, the associated fluxes and scaling trends in a rotor wake. Phys Fluids 17:085102

Crook AJ, Greitzer EM, Tan CS, Adamczyk JJ (1993) Numerical-simulation of compressor endwall and casing treatment flow phenomena. J Turbomach 115:501–512

Cumpsty NA (1989) Compressor aerodynamics. Longman Scientific & Technical, England (co published with John Wiley and Sons)

Denton JD (1993) The 1993 IGTI scholar lecture—loss mechanisms in turbomachines. J Turbomach 115:621–656

Farrell KJ, Billet ML (1994) A correlation of leakage vortex cavitation in axial-flow pumps. J Fluid Eng ASME 116:551–557

Fukano T, Jang CM (2004) Tip clearance noise of axial flow fans operating at design and off-design condition. J Sound Vib 275:1027–1050

Furukawa M, Inoue M, Saiki K, Yamada K (1999) The role of tip leakage vortex breakdown in compressor rotor aerodynamics. J Turbomach 121:469–480

Gbadebo SA, Cumpsty NA, Hynes TP (2005) Three-dimensional separations in axial compressors. J Turbomach 127:331–339

Gbadebo SA, Cumpsty NA, Hynes TP (2007) Interaction of tip clearance flow and three-dimensional separations in axial compressors. J Turbomach 129:679–685

Gerolymos GA, Vallet I (1999) Tip-clearance and secondary flows in a transonic compressor rotor. J Turbomach 121:751–762

Gourdain N, Leboeuf F (2009) Unsteady simulation of an axial compressor stage with casing and blade passive treatments. J Turbomach 131:021013

Guemmer V, Goller M, Swoboda M (2008) Numerical investigation of end wall boundary layer removal on highly loaded axial compressor blade rows. J Turbomach 130:011015

Hall MG (1972) Vortex breakdown. Annu Rev Fluid Mech 4:195

Hall EJ, Delaney RA (1994) Aerodynamic analysis of compressor casing treatment with a 3-D Navier-Stokes solver 30th AIAA, ASME, SAE, and ASEE, Joint Propulsion Conference and Exhibit. Indianapolis, IN

Hathaway MD (2007) Passive endwall treatments for enhancing stability NASA/TM—2007-214409 and ARL–TR–3878

Houghton T, Day I (2011) Enhancing the stability of subsonic compressors using casing grooves. J Turbomach 133:021007

Hoying DA, Tan CS, Vo HD, Greitzer EM (1999) Role of blade passage flow structures in axial compressor rotating stall inception. J Turbomach 121:735–742

Inoue M, Kuroumaru M, Tanino T, Yoshida S, Furukawa M (2001) Comparative studies on short and long length-scale stall cell propagating in an axial compressor rotor. J Turbomach 123:24–30

Khalid SA, Khalsa AS, Waitz IA et al (1999) Endwall blockage in axial compressors. J Turbomach 121:499–509

Kosyna F, Goltz I, Stark U (2005) Flow structure of an axial-flow pump from stable operation to deep stall proceedings of 2005 ASME fluids engineering division summer meeting, FEDSM2005. Houston, TX. Paper No. FEDSM2005-77350, 71389-71396

Laborde R, Chantrel P, Mory M (1997) Tip clearance and tip vortex cavitation in an axial flow pump. J Fluid Eng ASME 119:680–685

Lakshminarayana B (1970) Methods of predicting tip clearance effects in axial flow turbomachinery. J Basic Eng ASME 92:467

Lakshminarayana B (1996) Fluid dynamics and heat transfer of turbomachinery. Wiley, London

Lakshminarayana B, Davino R, Pouagare M (1982) 3-Dimensional flow field in the tip region of a compressor rotor passage. 2. Turbulence properties. J Eng Power ASME 104:772–781

Leibovich S (1978) Structure of vortex breakdown. Annu Rev Fluid Mech 10:221–246

Li YS, Cumpsty NA (1991a) Mixing in axial-flow compressors. 1. Test facilities and measurements in a 4-stage compressor. J Turbomach 113:161–165

Li YS, Cumpsty NA (1991b) Mixing in axial-flow compressors. 2. Measurements in a single-stage compressor and a duct. J Turbomach 113:166–174

Liu BJ, Wang HW, Liu HX, Yu HJ, Jiang HK, Chen MZ (2004) Experimental investigation of unsteady flow field in the tip region of an axial compressor rotor passage at near stall condition with stereoscopic particle image velocimetry. J Turbomach 126:360–374

Mailach R, Lehmann I, Vogeler K (2001) Rotating instabilities in an axial compressor originating from the fluctuating blade tip vortex. J Turbomach 123:453–460

McCarter AA, Xiao XW, Lakshminarayana B (2001) Tip clearance effects in a turbine rotor: part II—velocity field and flow physics. J Turbomach 123:305–313

Miorini RL, Wu H, Katz J (2011) The internal structure of the tip leakage vortex within the rotor of an axial waterjet pump. J Turbomach 134(3):031018

Muthanna C, Devenport WJ (2004) Wake of a compressor cascade with tip gap, part 1: mean flow and turbulence structure. AIAA J 42:2320–2331

Ortega JM, Bristol RL, Savas O (2003) Experimental study of the instability of unequal-strength counter-rotating vortex pairs. J Fluid Mech 474:35–84

Oweis GF, Ceccio SL (2005) Instantaneous and time averaged flow fields of multiple vortices in the tip region of a ducted propulsor. Exp Fluids 38:615–636

Palafox P, Oldfield MLG, LaGraff JE, Jones TV (2008) PIV maps of tip leakage and secondary flow fields on a low-speed turbine blade cascade with moving end wall. J Turbomach 130:011001

Pouagare M, Galmes JM, Lakshminarayana B (1985) An experimental-study of the compressor rotor blade boundary-layer. J Eng Gas Turb Power 107:364–373

Prasad AK (2000) Stereoscopic particle image velocimetry. Exp Fluids 29:103–116

Roth G, Katz J (2001) Five techniques for increasing the speed and accuracy of piv interrogation. Meas Sci Technol 12:238–245

Roth G, Mascenik DT, Katz J (1999) Measurements of the flow structure and turbulence within a ship bow wave. Phys Fluids 11:3512–3523

Saffman PG (1992) Vortex dynamics. Cambridge University Press, Cambridge

Schnell R, Voges M, Monig R, Muller MW, Zscherp C (2011) Investigation of blade tip interaction with casing treatment in a transonic compressor-part II: numerical results. J Turbomach 133:011008

Schrapp H, Stark U, Goltz I, Kosyna G, Bross S (2004) Structure of the rotor tip flow in a highly-loaded single-stage axial-flow pump approaching stall proceedings of the ASME heat transfer/fluids engineering summer conference 2004, HT/FED 2004. Charlotte, NC, pp 307–312

Shabbir A, Adamczyk JJ (2005) Flow mechanism for stall margin improvement due to circumferential casing grooves on axial compressors. J Turbomach 127:708–717

Shuba BH (1983) An investigation of tip-wall vortex cavitation in an axial-flow pump. Master Thesis, The Pennsylvania State University, Dept. of Aerospace Engineering

Smith GDJ, Cumpsty NA (1984) Flow phenomena in compressor casing treatment. J Eng Gas Turb Power 106:532–541

Soranna F, Chow YC, Uzol O, Katz J (2006) The effect of inlet guide vanes wake impingement on the flow structure and turbulence around a rotor blade. J Turbomach 128:82–95

Soranna F, Chow YC, Uzol O, Katz J (2008) Turbulence within a turbomachine rotor wake subject to nonuniform contraction. AIAA J 46:2687–2702

Soranna F, Chow YC, Uzol O, Katz J (2010) The effects of inlet guide vane-wake impingement on the boundary layer and the near-wake of a rotor blade. J Turbomach 132:041016

Stauter RC (1993) Measurement of the 3-dimensional tip region flow-field in an axial compressor. J Turbomach 115:468–476

Tan CS, Day I, Morris S, Wadia A (2010) Spike-type compressor stall inception, detection, and control. Annu Rev Fluid Mech 42:275–300

Uzol O, Chow YC, Katz J, Meneveau C (2002) Unobstructed particle image velocimetry measurements within an axial turbo-pump using liquid and blades with matched refractive indices. Exp Fluids 33:909–919

Uzol O, Chow YC, Katz J, Meneveau C (2003) Average passage flow field and deterministic stresses in the tip and hub regions of a multistage turbomachine. J Turbomach 125:714–725

Vo HD, Tan CS, Greitzer EM (2008) Criteria for spike initiated rotating stall. J Turbomach 130:011023

Voges M, Schnell R, Willert C, Monig R, Muller MW, Zscherp C (2011) Investigation of blade tip interaction with casing treatment in a transonic compressor-part I: particle image velocimetry. J Turbomach 133:011007

Wang Y, Devenport WJ (2004) Wake of a compressor cascade with tip gap, part 2: effects of endwall motion. AIAA J 42:2332–2340

Wenger CW, Devenport WJ, Wittmer KS, Muthanna C (2004) Wake of a compressor cascade with tip gap, part 3: two-point statistics. AIAA J 42:2341–2346

Wieneke B (2005) Stereo-PIV using self-calibration on particle images. Exp Fluids 39:267–280

Wilke I, Kau HP (2004) A numerical investigation of the flow mechanisms in a high pressure compressor front stage with axial slots. J Turbomach 126:339–349

Wu H, Miorini RL, Katz J (2011) Measurements of the tip leakage vortex structures and turbulence in the meridional plane of an axial water-jet pump. Exp Fluids 50:989–1003

Xiao XW, McCarter AA, Lakshminarayana B (2001) Tip clearance effects in a turbine rotor: part I—pressure field and loss. J Turbomach 123:296–304

You D, Wang M, Moin P, Mittal R (2006) Effects of tip-gap size on the tip-leakage flow in a turbomachinery cascade. Phys Fluids 18:105102

Yu XJ, Liu BJ (2007) Stereoscopic PIV measurement of unsteady flows in an axial compressor stage. Exp Therm Fluid Sci 31:1049–1060